APL Materials

Self-supported AlFeNiCoMo high-entropy alloy with micropillar array structure for efficient oxygen evolution reaction

Cite as: APL Mater. **10**, 101106 (2022); https://doi.org/10.1063/5.0117046
Submitted: 30 July 2022 • Accepted: 19 September 2022 • Published Online: 24 October 2022

Qianqian Wang, Yongjie Li, Yiyuan Yang, et al.

Self-supported AlFeNiCoMo high-entropy alloy with micropillar array structure for efficient oxygen evolution reaction

Cite as: APL Mater. 10, 101106 (2022); doi: 10.1063/5.0117046
Submitted: 30 July 2022 • Accepted: 19 September 2022 •
Published Online: 24 October 2022

Qianqian Wang,[1,2] Yongjie Li,[1] Yiyuan Yang,[1] Xinyue Zhang,[1] Yangbin Guo,[1] Zhe Jia,[1] and Baolong Shen[1,a)]

AFFILIATIONS

[1] School of Materials Science and Engineering, Jiangsu Key Laboratory for Advanced Metallic Materials, Southeast University, Nanjing 211189, China
[2] School of Materials Science and Engineering, Jiangsu Key Laboratory of Advanced Structural Materials and Application Technology, Nanjing Institute of Technology, Nanjing 211167, China

Note: This paper is part of the Special Topic on Design and Development of High Entropy Materials.
[a)] **Author to whom correspondence should be addressed:** blshen@seu.edu.cn

ABSTRACT

The development of low-cost and efficient electrocatalysts for oxygen evolution reaction (OER) is crucial for the application of hydrogen energy. In this work, a self-supported AlFeCoNiMo high entropy alloy with a uniformly distributed micropillar array structure on the surface is prepared by melt spinning followed by dealloying. The catalyst exhibits a low overpotential of 228, 265, and 318 mV to drive the current densities of 10, 100, and 1000 mA/cm^2, a small Tafel slope of 51 mV/dec, and excellent long-term stability for 30 h in 1.0M KOH electrolyte for OER. The high catalytic activity is attributed to the unique micropillar array with rich active sites and the synergistic effect between multiple metallic elements. The good stability of the catalyst results from the steady micropillar array structure and the formation of oxyhydroxides on the surface during long-term catalysis. This work provides a facile and scalable method for the preparation of self-supported, low-cost, and high-performance OER electrocatalysts.

I. INTRODUCTION

The global climate change caused by greenhouse gas emissions leads to the urgency of developing clean, renewable, and reliable energy resources, such as solar, wind, and hydrogen.[1] Among them, hydrogen is more prevalent as it provides continuous power supplies. Compared with the hydrogen produced by burning fossils, water electrolysis is regarded as the most promising approach to obtaining hydrogen due to its relatively simple instrument requirement and no carbon emission as a by-product.[2,3] The anodic oxygen evolution reaction (OER) involved in water electrolysis is a multi-proton coupled process with slow kinetics, which seriously hinders the overall efficiency of hydrogen production.[4,5] At present, noble metal-based catalysts, such as IrO_2 and RuO_2, are commercially used to improve OER efficiency.[6] However, the scarcity of noble metals leads to the high cost of catalysts, which is one of the reasons that limit the industrial application of water electrolysis. Therefore, it is urgent to develop low-cost, efficient, and durable catalysts to accelerate the OER reaction kinetics, thereby improving the overall hydrogen production efficiency from water electrolysis.

High-entropy alloy (HEA), which is a kind of multiple principle component alloys with ordered crystalline structure but disordered elemental distribution, has attracted a great deal of research interest in many research fields because of its unique physical and chemical properties.[7–9] Specifically, HEA has been reported as a promising electrocatalyst in many electrochemical reaction systems.[9–11] The large lattice distortion in HEA not only makes the atoms in a thermodynamically metastable state and generates more lattice defects on the surface to expose abundant active sites but also delayed the diffusion of atoms to maintain a stable structure in the strong acidic or alkaline environment.[12,13] Therefore, both the catalytic efficiency

and the stability of the HEA electrocatalyst are potentially better than that of traditional alloys.[14] Furthermore, the multiple principle components guarantee the tunable electronic structure of the HEA, which makes the M–O and M–OH bonds on the surface have suitable adsorption energies.[15,16] The 3*d* transition metals (e.g., Fe, Co, and Ni), with low cost and tunable electronic structure, are widely used as constituent elements for OER catalysts, such as NiFe layered double hydroxides (LDH) and metal–organic frameworks (MOF).[17–22] Recently, HEAs composed of 3*d* transition metals have been reported to exhibit high performance in the OER process. The synergistic effect between the components guarantees its good intrinsic catalytic activity.[23,24]

Furthermore, it has been proved that dealloying is an effective and controllable strategy to further improve the activity of catalytic materials.[25–27] The dealloying process not only tunes the surface morphology but also optimizes the internal electronic structure and thus affects the electrochemical performance of the catalysts.[28,29] The core–shell nanostructure obtained by dealloying the eutectic high-entropy alloy $FeCoNiCrNb_{0.5}$ in the acidic solution offered excellent OER performance with an overpotential of 288 mV at a current density of 10 mA/cm^2 in 1.0M KOH electrolyte, due to the large active surface area.[30] A continuous nanoporous structure fabricated by surface dealloying AlFeCoNiCr ribbon provided an outstanding OER activity in alkaline media.[31] Moreover, the unique AlNiCoRuMo nanowires structure obtained by dealloying treatment exhibited a high electrocatalytic activity as commercial RuO_2 for OER.[32] In addition, a freestanding nanoporous structure fabricated by electrochemical dealloying NiCoFeMoMn ribbons showed high OER catalytic activity in alkaline media with a low overpotential of 350 mV to achieve the current density of 1000 mA/cm^2 and a small Tafel slope of 37 mV/dec.[33] Designing HEA with a dual-phase structure not only helps to obtain nanoporous structure but also provides an opportunity to construct high-entropy intermetallic (HEI) as an active electrocatalyst. A unique HEI with a dendrite-like porous $L1_2$-type ordered structure is produced after dealloying FeCoNiAlTi and shows a comparable activity to the noble catalyst in alkalinity for hydrogen production.[34]

In this work, a free-standing AlFeCoNiMo HEA catalyst with a uniformly distributed micropillar array structure on the surface was prepared by melt spinning technique followed by a one-step chemical dealloying method. The catalyst exhibits a low overpotential of 228 mV at 10 mA/cm^2, a small Tafel slope of 35 mV/dec, and excellent long-term stability for 30 h in 1.0M KOH electrolyte. Specifically, the catalyst shows low overpotentials even at high current densities, i.e., 265 mV at 100 mA/cm^2 and 318 mV at 1000 mA/cm^2, indicating good reliability at a wide current density range in industrial applications. The high catalytic activity comes from the large specific surface area and the synergistic effect of multiple elements, and the excellent stability results from the steady micropillar structure and formation of oxyhydroxides on the surface. This work provides a facile and scalable strategy to prepare a free-standing, low-cost, efficient, and stable OER electrocatalyst.

II. EXPERIMENTAL

The HEA ingots with a composition (at. %) of $AlFeCoNi_3Mo_{0.2}$ were prepared by arc melting the mixed aluminum (Al), iron (Fe), cobalt (Co), nickel (Ni), and molybdenum (Mo) particles (purity higher than 99.9%) under high-purity argon protection. The ingot was remelted four times to assure the even distribution of the elements. The AlFeCoNiMo HEA ribbons with a thickness of ~30 μm and a width of 2 mm were prepared by melt spinning under a high-purity argon atmosphere, and the linear speed of the melt spinning was 40 m/s. The ribbons were cut into 20 mm in length and then dealloyed in 1.0M HNO_3 solution. The dealloyed ribbons were rinsed three times with deionized water and then alcohol to remove residual chemical reagents on the surface before electrochemical tests. Based on the time of dealloying (0, 5, 10, 15, and 18 min), the ribbons are named as-spun, DE-5, DE-10, DE-15, and DE-18, respectively.

The electrochemical properties of catalysts were investigated using an electrochemical workstation (Gamary Interface 1000) with a standard three electrode cell configuration at room temperature. A Pt sheet and a standard Hg/HgO electrode were used as the counter electrode and the reference electrode, respectively. 1.0M KOH solution was used as an electrolyte. The electrocatalytic activities were measured by linear sweep voltammetry (LSV) at a scan rate of 5 mV/s in the potential range from 1.2 to 1.65 V (vs RHE). The potential was calculated according to equation $E(\text{RHE}) = E(\text{Hg/HgO}) + 0.0591 \times \text{pH} + 0.098$ V. The polarization current densities were normalized by the geometric surface area. The Tafel slopes were derived from the linear region of the LSV polarization curves according to the equation ($\eta = b \times \log j + a$, where b represents the Tafel slope and j denotes the current density). Electrochemical impedance spectroscopy (EIS) was carried out from 10^{-1} to 10^5 Hz at an overpotential of 300 mV. To evaluate the electrochemical active surface areas (ECSAs), the cyclic voltammograms (CVs) were carried out within the non-faradaic potential region (1.323–1.383 V vs RHE) at scan rates ranging from 10 to 50 mV/s. The ECSA was obtained according to the equation $\text{ECSA} = C_{\text{dl}}/C_s$, where C_{dl} is the measured double-layer capacitance and C_s is the specific capacitance value of 0.040 mF/cm^2 in 1.0M KOH solution.[12] The electrocatalytic stability of the catalyst was measured by the chronopotentiometry test with a constant current density of 10 mA/cm^2.

The phases of the samples were analyzed using an x-ray diffraction (XRD, D8-Discover) instrument equipped with Cu-Kα (λ = 1.54 Å) radiation. The morphology and elemental distribution of the samples were analyzed by scanning electron microscopy (SEM, Zeiss Supra55) equipped with energy-dispersive x-ray spectroscopy (EDS). The nanostructure of the samples was analyzed by transmission electron microscopy (TEM, Tecnai G2 F3) equipped with selected area electron diffraction (SAED). The binding energies of the elements were obtained using an x-ray photoelectron spectroscopy (XPS, Thermo Fisher Nexsa) with an Al Kα (1486.6 eV) x-ray source. The calibration was carried out using C 1s (284.80 eV) as charge compensation.

III. RESULTS AND DISCUSSION

The TEM image of the as-spun $AlFeCoNi_3Mo_{0.2}$ ribbon is shown in Fig. 1(a), exhibiting a dual-phase structure with one phase of large grains in micro-scale and the other phase existing at the grain boundaries. The SAED patterns of the two phases are analyzed and shown in Figs. 1(b) and 1(c), respectively. As super lattice is observed on the SAED pattern in Fig. 1(b), the micro-scale grains are

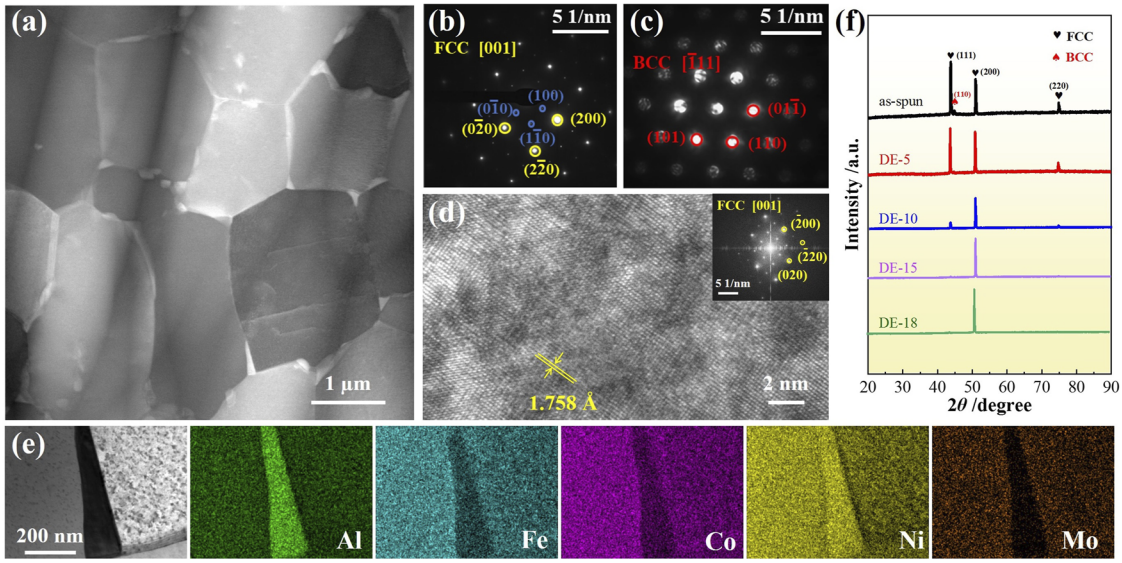

FIG. 1. Microstructure analyses of the as-spun $AlFeCoNi_3Mo_{0.2}$ HEA. (a) TEM. SAED patterns of (b) the large grains and (c) the area between the large grains. (d) HRTEM of the large grain, inset is the FFT image. (e) HAADF and the EDS mapping. (f) XRD patterns of the as-spun and dealloyed HEAs.

identified as ordered face-centered cubic (FCC) crystalline structure $L1_2$, while the phase between the FCC grains are disordered body-centered cubic (BCC) crystalline structure. The HR-TEM image of the micro-scale grain is shown in Fig. 1(d). The d-spacing of the lattice is 1.758 Å, which is consistent with the (200) plane of the $L1_2$ phase. The FFT image of Fig. 1(d) is shown in the inset, further confirming the $L1_2$ structure. The composition of the two phases is analyzed by EDS, as shown in Fig. 1(e), indicating the $L1_2$ is a Fe, Co, and Mo rich phase, while the BCC phase has a higher concentration of Al and Ni. The phase separation may result from the largest negative mixing enthalpy (22 kJ/mol) of the Al–Ni atomic pair.

The as-spun $AlFeCoNi_3Mo_{0.2}$ ribbons were then dealloyed in 1.0M HNO_3 solution for 5, 10, 15, and 18 min and named DE-5, DE-10, DE-15, and DE-18, respectively. The evolutions of the phase structure of the $AlFeCoNi_3Mo_{0.2}$ ribbon during the dealloying process are analyzed by XRD, as shown in Fig. 1(f). The XRD pattern of the as-spun ribbon shows four peaks at 43.60°, 50.79°, 74.68°, and 44.50°, which are characteristics of the (111), (200), and (220) planes of the FCC phase and the (110) plane of the BCC phase, further confirming its dual-phase structure. Compared with the XRD pattern of the as-spun ribbon, the BCC phase is barely seen in the DE-5 sample and disappears after 10 min dealloying. The HRTEM image of DE-15 with the corresponding SAED pattern in Fig. S1 further confirms that the catalyst is composed of an ordered FCC phase, which is in accordance with the XRD results in Fig. 1(f). For the FCC phase, the diffraction intensity of the (200) plane is constant during the dealloying process, while the diffraction intensities of the (111) and (220) planes decrease continuously and disappear completely after 15 min. It indicates that with the increasing dealloying time, not only the BCC phase is dissolved but also the FCC phase is also dissolved from preferred crystalline planes. The quantitative compositions (at. %) of the FCC and BCC phases are obtained based on the EDS results in Fig. 1(e) and listed in Table S1. The FCC phase can be written as $Al_{8.3}Fe_{18.5}Co_{17.9}Ni_{52}Mo_3$, while the BCC phase is $Al_{16.6}Fe_{13.4}Co_{13.1}Ni_{56.3}Mo_{0.6}$. To compare the corrosion resistance of the two phases, the ingots with the above-mentioned compositions were prepared by arc melting and then cut into 15 × 8 × 2 mm^3 bulk for electrochemical tests. The potentiodynamic polarization tests of $Al_{8.3}Fe_{18.5}Co_{17.9}Ni_{52}Mo_3$ and $Al_{16.6}Fe_{13.4}Co_{13.1}Ni_{56.3}Mo_{0.6}$ were carried out in 1.0 M HNO_3 solution at room temperature. As shown in Fig. S2, the corrosion current density I_{corr} of the $Al_{8.3}Fe_{18.5}Co_{17.9}Ni_{52}Mo_3$ (FCC) sample (6.6×10^{-4} A/cm^2) is smaller than that of the $Al_{16.6}Fe_{13.4}Co_{13.1}Ni_{56.3}Mo_{0.6}$ (BCC) sample (5.9×10^{-3} A/cm^2). Moreover, the corrosion potential E_{corr} of the $Al_{8.3}Fe_{18.5}Co_{17.9}Ni_{52}Mo_3$ (FCC) sample (-3.7×10^{-2} V) is larger than that of the $Al_{16.6}Fe_{13.4}Co_{13.1}Ni_{56.3}Mo_{0.6}$ (BCC) sample (-1.1×10^{-1} V). The FCC phase has better corrosion resistance than the BCC phase, and this can be attributed to the higher concentration of Mo in the FCC phase. Thus, the BCC phase in $AlFeCoNi_3Mo_{0.2}$ HEA can be preferentially dissolved to construct a nanoporous structure to provide more active reaction sites on the surface.

The surface morphology of the as-cast and dealloyed $AlFeCoNi_3Mo_{0.2}$ HEA ribbons are analyzed by SEM and shown in Figs. 2(a)–2(e), and the SEM images of corresponding cross sections of the dealloyed ribbons are presented in the insets. The surface of the as-spun ribbon is relatively smooth. Connecting pores appear on the surface after 5 min dealloying, which comes from the dissolved BCC phase at the grain boundaries. Correspondingly, a thin corroded layer appears on the cross section. The size of the pores on the surface is larger on the surface of DE-10 than that of DE-5, and the depth of the corroded layer increases to 3–4 μm observed from the cross section. This is consistent with the gradual disappearance of the (111) and (220) planes of the FCC phase as shown in Fig. 1(f). After 15 min dealloying, micropillar arrays can be observed on the

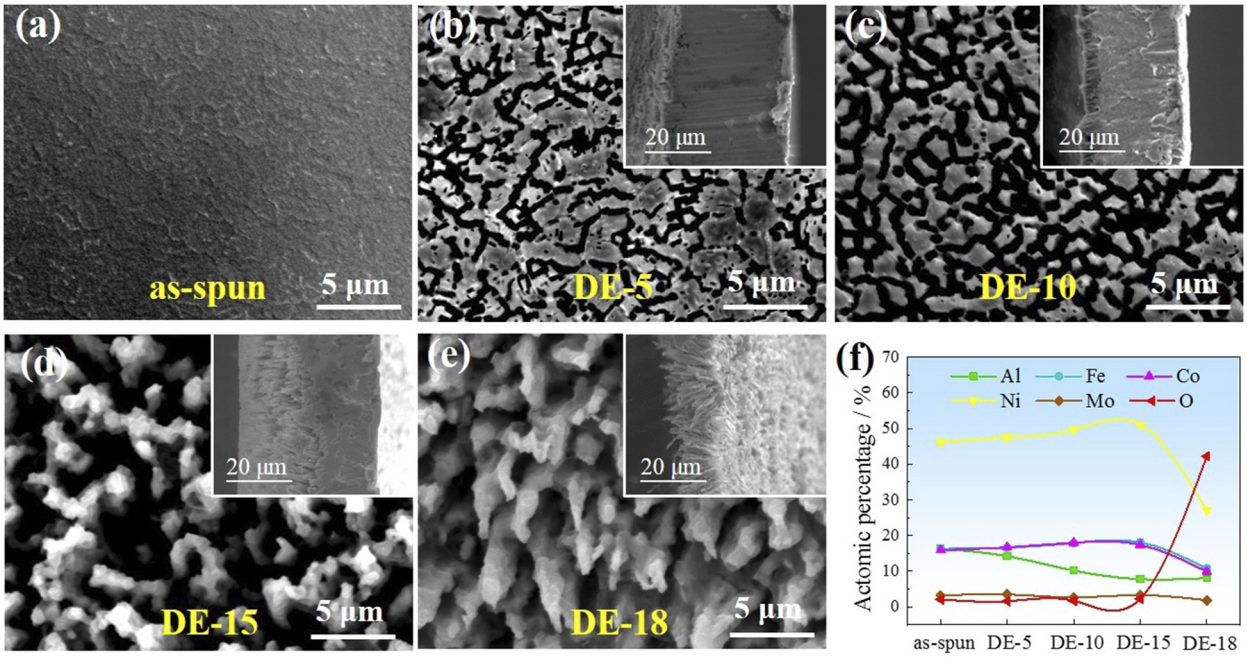

FIG. 2. Surface morphologies analyzed by SEM for the as-spun and dealloyed HEAs. (a) as-spun. (b) DE-5. (c) DE-10. (d) DE-15. (e) DE-18. The insets are corresponding cross sections. (f) The surface composition (at. %) analyzed by EDS.

surface. The porous area is much larger than the BCC phases, suggesting the FCC phase is also dissolved. The cross section of DE-15 shows a micropillar array structure on the surface with some dense matrix left in the middle. After 18 min of dealloying, the diameters of the micropillar increase. Observed from the cross section, the ribbon has been corroded through and is only composed of micropillar arrays. The disappearance of the intermediate matrix layer not only limits the conductivity but also makes the ribbon too brittle to be self-supported.

The variation of surface composition during the dealloying process is analyzed by EDS and shown in Fig. 2(f). During the dealloying process for the first 15 min, because of the dissolvent of the BCC phase, the atomic percentage of Al element decreases from 16.4% in the as-spun ribbon to 7.8% in DE-15, and a slight increase in the concentration of Fe, Co and Ni elements is observed due to the decrease of Al concentration. No obvious variation of the Mo concentration is observed because of its relatively low concentration in the as-spun ribbon, and O is barely detected. After dealloyed for 18 min, a substantial increase of the O is observed, indicating oxidation of the ribbon occurred. Significant reduction of the metallic elements Fe, Co, Ni, and Mo is observed, while the Al concentration remains unchanged. This suggests that the formation of aluminum oxides covering the micropillars may explain the enlarged micropillars in the DE-18 sample, as shown in Fig. 2(e). The coverage of the Fe, Co, Ni, and Mo elements by aluminum oxides in the DE-18 ribbon jeopardizes its conductivity and activity.

The surface chemistry and electronic structure of the as-spun and DE-15 ribbons were analyzed by XPS. The XPS spectra of binding energies of Al 2p ($2p_{3/2}$ and $2p_{1/2}$), Fe 2p ($2p_{3/2}$ and $2p_{1/2}$), Co 2p ($2p_{3/2}$ and $2p_{1/2}$), Ni 2p ($2p_{3/2}$ and $2p_{1/2}$), Mo 3d ($2d_{5/2}$ and $2d_{3/2}$), and O 1s are shown in Fig. 3, and the values are summarized in Table S2. The XPS spectra of the as-spun ribbon show the existence of Al, Fe, Ni, Co, Mo, and O elements on the surface. The existence of O is attributed to surface oxidation during the sample preparation process. As illustrated in Fig. 3(a), the Al $2p_{3/2}$ spectrum is deconvoluted into two peaks. The peak at 74.94 eV corresponds to the Al^{3+}, and the peak at 72.51 eV is indexed to Al^0. For Al $2p_{1/2}$, only one peak at 77.66 eV can be detected, and it corresponds to Al^{3+}. After dealloying treatment for 15 min, the binding energies of Al $2p_{3/2}$ show a negative shift, i.e., 74.21 eV for Al^{3+} and 72.14 eV for Al^0. The signal from Al $2p_{1/2}$ is too weak to be detected. Moreover, the amount of Al in DE-15 is much smaller than that in the as-spun ribbon. As shown in Fig. 3(b), the Fe $2p_{3/2}$ peaks are deconvoluted into two peaks, the peaks located at 707.2 and 712.3 eV are characteristics of Fe^0 and Fe^{3+} species, respectively. In addition, only the peak from Fe^0 (720.4 eV) is detected for Fe $2p_{1/2}$. It was found that the Fe^0 evolved to Fe^{2+} and Fe^{3+} completely on the surface of DE-15, suggesting that the Fe sites in DE-15 are ready to accept the hydroxyl groups and likely to promote the catalytic activity.[23] Moreover, the binding energies of Fe^{3+} species shift from 712.3 to 712.8 eV. Similarly, compared with the as-spun ribbon, no peak from Co^0 is observed on the surface of DE-15, while the intensities of the Co^{3+} species located at 781.4 eV increase tremendously. As shown in Fig. 3(d), the Ni $2p_{3/2}$ spectrum of the as-spun catalyst can be fitted into three peaks, which are Ni^0 at 853.0 eV, Ni^{2+} at 853.9 eV, and their satellite peak at 858.6 eV. The Ni $2p_{1/2}$ are deconvoluted into two peaks for Ni^0 (870.3 eV) and Ni^{3+} (874.5 eV), respectively. Likewise, Ni^0 is greatly reduced, and the intensity of Ni^{3+} increases significantly after dealloying

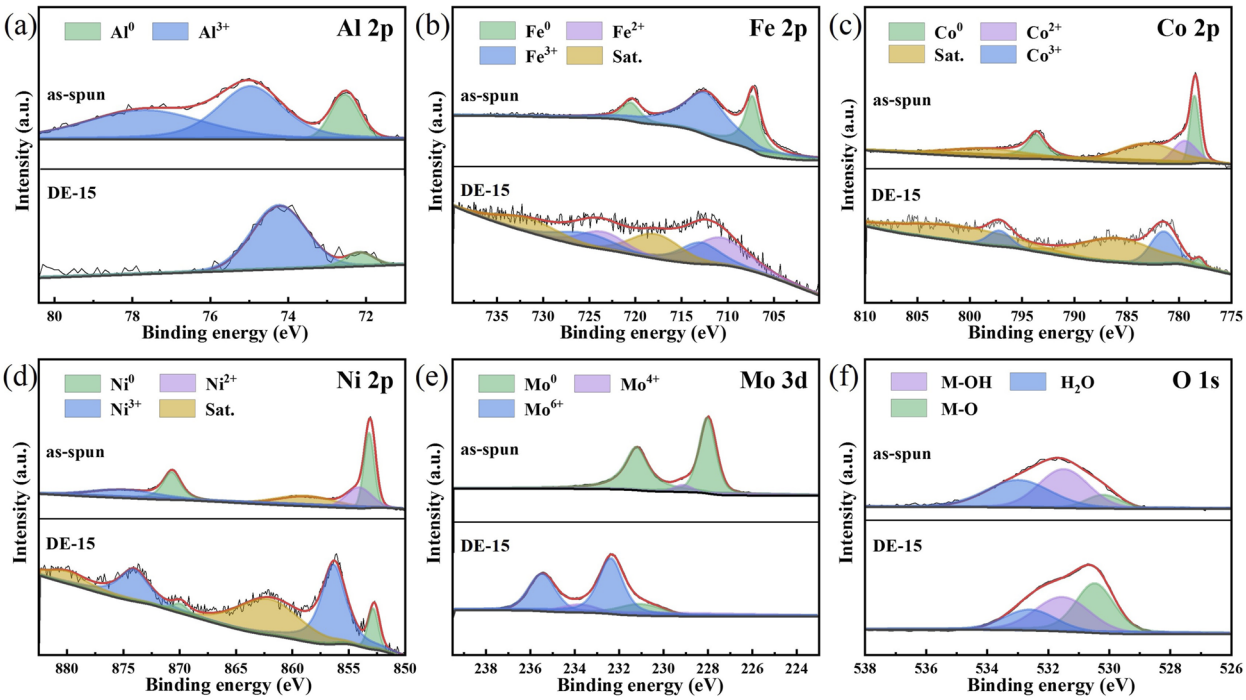

FIG. 3. XPS analyses of the as-spun and DE-15 samples. (a) Al 2p. (b) Fe 2p. (c) Co 2p. (d) Ni 2p. (e) Mo 3d. (f) O 1s.

treatment. In Fig. 3(e), there is basically only Mo^0 in the as-spun ribbon, but the oxidation state species of Mo replaces Mo^0 after dealloying treatment. It was reported that Mo with high valence can reduce the adsorption energy of the intermediates by modifying the electronic structure of transition metals and thus accelerate the OER process.[35] Based on the above results, the 15 min dealloying treatment makes metallic elements on the surface undergo an intense electron transfer process. The positive shift of the binding energy indicates that the Fe atoms provide electrons to their neighbors, and thus, the electron density around Fe atoms decreases, while the binding energy of Co, Ni, and Mo shift negatively, indicating that these atoms gain electrons, which would increase the electron density around them. Therefore, the electronic structure of the HEA is optimized, making an improvement in the electrocatalytic performance.[36] In addition, as shown in Fig. 3(f), analyses of the O 1s show that the DE-15 catalyst possesses higher content of metal oxides and hydroxides than the as-spun HEA, which may contribute to the improvement of OER catalytic activity in DE-15, as metal oxides and hydroxides are believed to provide more reaction active sites during OER.[37]

The OER electrocatalytic performance of the as-spun and dealloyed ribbons is investigated in 1.0M KOH electrolyte. As shown by the LSV scans in Fig. 4(a), to achieve a current density of 10 mA/cm^2, it takes the as-spun ribbon an overpotential of 307 mV, while only 257, 249, 228, and 271 mV are required for DE-5, DE-10, DE-15, and DE-18 ribbons. The HEA shows the best OER activity after dealloying for 15 min. As shown in Fig. 4(b), DE-15 also shows high activity in high current densities, as the overpotentials for DE-15 to achieve 100, 500, and 1000 mA/cm^2 are only 265, 300, and 318 mV, which leads to great potential in industrial applications.[38] The Tafel slopes derived from the corresponding LSV curves are shown in Fig. 4(c). With an increase in dealloying time from 0 to 15 min, the Tafel slope reduces from 72 to 35 mV/dec and then increases to 53 mV/dec for DE-18. This result indicates that the fastest OER reaction kinetics is achieved in DE-15. As shown in Fig. 4(d), the EIS measurements are carried out to evaluate the electron transport ability of the samples. The Nyquist plots of the as-spun and dealloyed ribbons are fitted by equivalent circuits. It was found that the DE-15 catalyst presents a smaller semicircle diameter compared to other samples, namely, the charge-transfer resistance of the DE-15 catalyst (2.3 Ω) is much smaller than that of the as-spun (15.8 Ω), DE-5 (4.9 Ω), DE-10 (3.3 Ω), and DE-18 (4.1 Ω) samples. This result reveals the excellent electron transport on the conductive surface of the DE-15 catalyst. The electrochemical surface area (ECSA) of the samples was evaluated by the double-layer capacitance (C_{dl}) obtained from the cyclic voltammetry curves scanned at different rates (Fig. S3). As shown in Fig. 4(e), the C_{dl} value for the DE-15 catalyst is 0.91 mF/cm^2, which is approximately twenty times that for the as-spun catalyst (0.04 mF/cm^2), indicating a sharp increase in the quantity of active sites after the formation of the micropillar arrays on the surface. The largest ECSA of DE-15 contributes to its excellent OER activity. In addition to the electrochemical activity, the stability of catalysts is also a key factor for industrial applications. As shown in Fig. 4(f), the DE-15 catalyst shows a negligible increase of the overpotential after 30 h chronoamperometry measurement at a potential of 1.46 V (vs RHE), indicating its good durability in

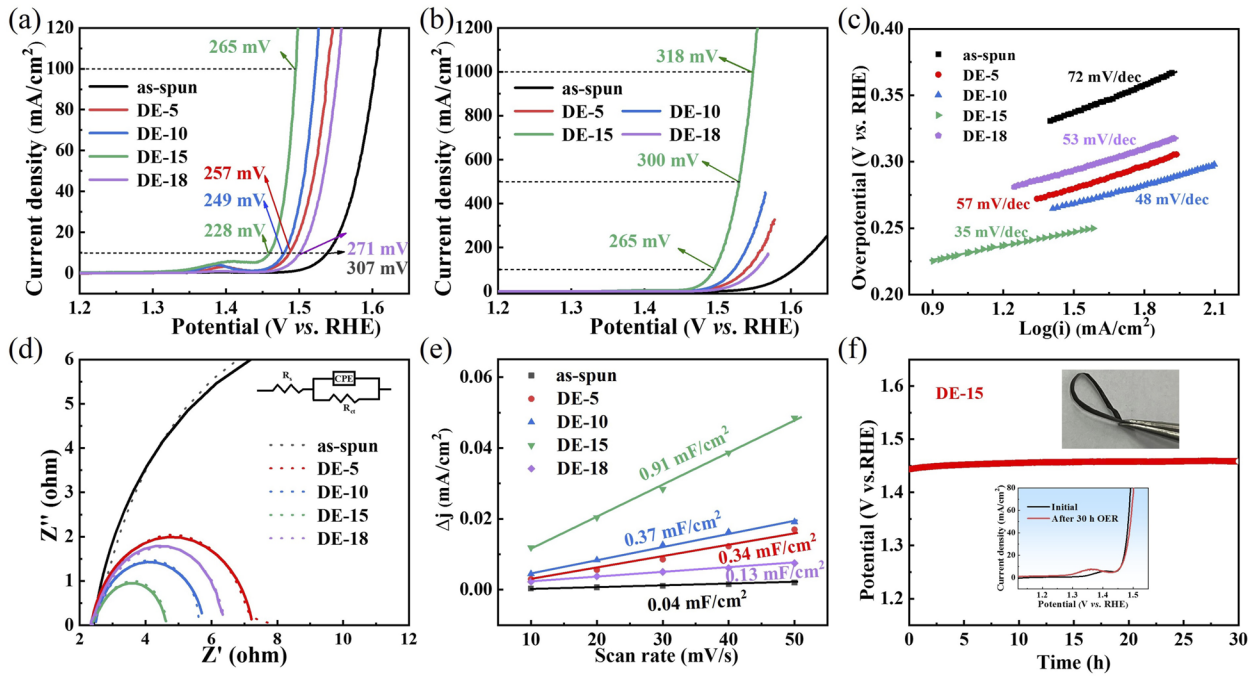

FIG. 4. Electrochemical properties of the catalysts in 1.0M KOH. (a) LSV polarization curves (*IR*-corrected) at low current densities. (b) LSV polarization curves (*IR*-corrected) at high current densities. (c) Tafel slopes. (d) Nyquist plots measured at an overpotential of 300 mV. (e) Plots of capacitive current as a function of scan rates for electrocatalysts. (f) Chronopotentiometric curve at a potential required to afford 10 mA/cm^2 of DE-15, the inset (above) shows that the good flexibility is kept for the ribbon after 30 h OER catalysis, and the inset (below) shows the polarization curves (*IR*-corrected) of DE-15 for initial OER catalysis and after continuous 30 h OER catalysis.

alkaline media. As shown in the inset, the LSV polarization curves of the DE-15 catalyst for the initial OER and after 30 h continuous OER almost overlap, further revealing the catalyst maintains high catalytic activity after long-term use. Moreover, the ribbon remains flexible after the 30 h OER test. The above results suggest that DE-15 is a high-performance self-supporting OER catalyst with high efficiency, good stability, and excellent flexibility.

To evaluate the catalytic performance of DE-15, the Tafel slope and overpotential (@ 10 mA/cm^2 in 1.0M KOH electrolyte) of DE-15 are compared with the representative non-precious metal OER electrocatalysts that have been reported recently, as shown in Fig. 5. Details of the catalysts, including constituents, morphology, overpotentials, and Tafel slopes, are listed in Table S3. The DE-15 has a lower overpotential and Tafel slope than most of the catalysts, including LDH, MOF, metallic glass (MG), perovskite, HEA, and RuO_2. It is noteworthy that MOF, LDH, and perovskite are prepared by the wet chemistry method and need to be bonded to the electrodes. These catalysts are easy to fall off from the electrodes at high current densities. In comparison, the DE-15 catalyst prepared by melt spinning and dealloying, a simple and scalable metallurgical preparation technique, is self-supported and may be directly used as an electrode.

To uncover the origin of the good stability of DE-15, the microstructure and electronic structure of this catalyst after 30 h OER are analyzed. The binding energies of the elements on DE-15 are investigated by XPS, and the results are shown in Fig. S4 and Table S2. After long-term OER, the metallic elements only retain the highest oxidation state, and the metal state and the low-valent oxidation state disappear completely, suggesting oxyhydroxide is formed on the surface. Figure 6(a) shows the SEM image of DE-15 after 30 h OER, and the micropillar array structure is maintained, which may result from the sluggish diffusion effect of HEA. The micropillar array keeps a large number of active sites for OER and enables it to maintain high catalytic activity for a long time. Furthermore, as shown in Fig. 6(b), the SAED pattern of the DE-15 after 30 h OER confirms the existence of (Fe, CO, Ni)OOH, as diffraction rings from the planes (105), (108), and (116) of (Fe, CO, Ni)OOH can be clearly observed. The HR-TEM of this sample is shown in Fig. 6(c), and the lattice spacing is ~2.03 Å, which can be assigned to the plane (105) for crystalline (Fe, CO, Ni)OOH. This result is consistent with the appearance of high-valence oxyhydroxides in XPS spectra in Fig. S4. It is well known that Ni, Fe, and Co-based alloys and oxides tend to transform into Ni, Fe, and Co-oxyhydroxides, such as NiOOH, FeOOH, and CoOOH, in the alkaline electrolyte during water electrolysis, which are active sites for OER to attract hydroxyl groups owing to its hydrophilicity.[15] The slow kinetics of OER is mainly attributed to the lack of intermediates, including MOH*, MO*, and MOOH*. In this work, oxyhydroxides are formed during the long-term OER, providing abundant intermediates (MOOH) and active sites for OER, thus accelerating the OER reaction kinetics. Moreover, the EDS analysis of the DE-15 catalyst after long-term OER reveals a homogeneous distribution of the constituents, as

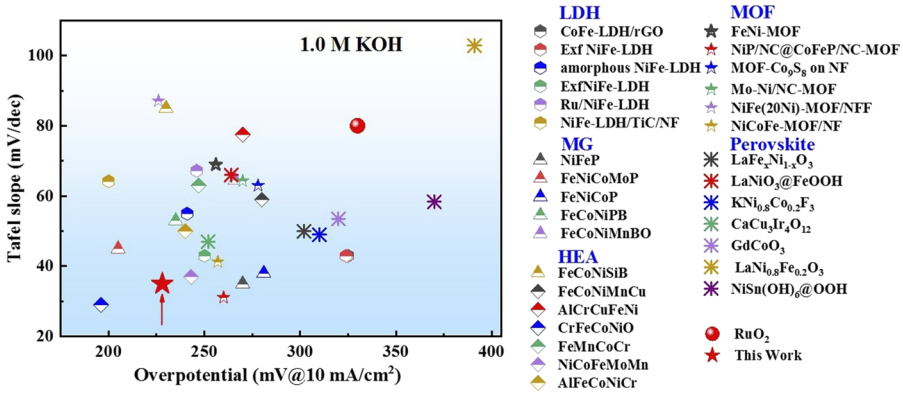

FIG. 5. Comparison of the overpotential (at a current density of 10 mA/cm^2) and Tafel slope for representative non-precious metal OER catalysts in 1.0M KOH electrolytes.

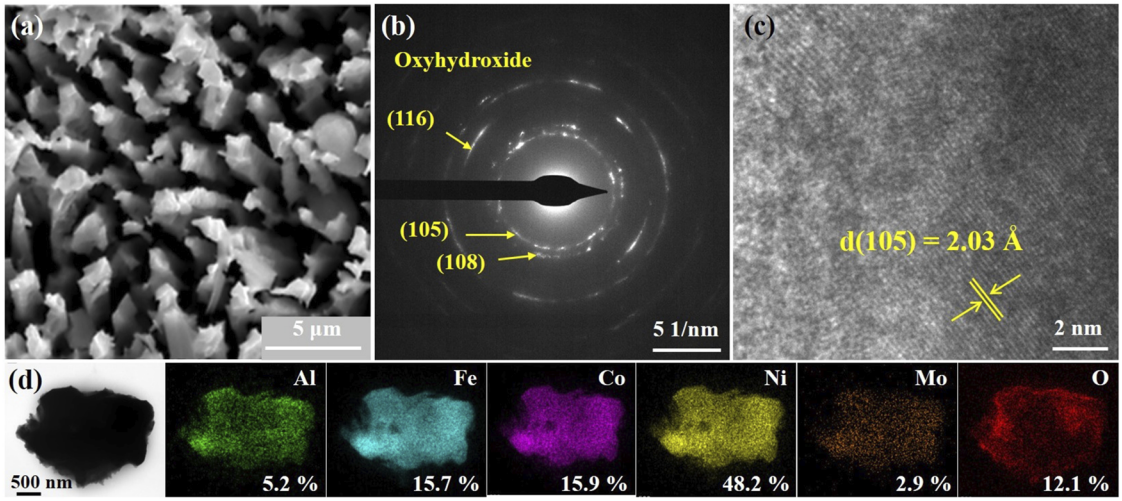

FIG. 6. Microstructure of the DE-15 after 30 h OER. (a) SEM. (b) SAED pattern, the inset is the TEM image. (c) HR-TEM. (d) Element distribution.

shown in Fig. 6(d), and the high concentration of O element further demonstrates the formation of surface oxyhydroxides. Based on the above results, the structural and catalytic stability of DE-15 comes from the formation of intermediate oxyhydroxides during the long-term OER and the slow diffusion effect of high entropy alloys.

IV. CONCLUSION

In summary, a self-supported $AlFeCoNi_3Mo_{0.2}$ HEA electrocatalyst with a uniform micropillar array structure on the surface was prepared by melt spinning followed by dealloying. The catalyst exhibited excellent OER catalytic performance in 1.0M KOH electrolyte, exhibiting low overpotentials of 228, 265, and 318 mV to drive current densities of 10, 100, and 1000 mA/cm^2 with a small Tafel slope of 35 mV/dec and maintaining high catalytic activity over 30 h. The high catalytic activity comes from the improved specific surface area due to the unique micropillar array structure on the surface and the optimized electronic structure by the synergistic effect of multiple metallic elements. The catalyst showed good catalytic stability due to the maintained micropillar array structure and the formation of oxyhydroxides on the surface. In this work, a facile and scalable strategy to prepare low-cost, self-supported, efficient, and stable HEA electrocatalysts for the OER process in alkaline electrolytes is provided, which have a high potential to be used in industrial water electrolysis.

SUPPLEMENTARY MATERIAL

See the supplementary material for the supplementary figures and tables.

ACKNOWLEDGMENTS

This study was supported by the National Natural Science Foundation of China (Grant Nos. 52231005 and 52201174), and the Jiangsu Provincial Key Research and Development Program (Grant No. BE2021088).

AUTHOR DECLARATIONS

Conflict of Interest

The authors have no conflicts to disclose.

Author Contributions

Qianqian Wang: Investigation (lead); Writing – original draft (lead). **Yongjie Li**: Formal analysis (lead); Investigation (lead); Methodology (lead). **Yiyuan Yang**: Formal analysis (equal); Investigation (equal). **Xinyue Zhang**: Investigation (equal). **Yangbin Guo**: Investigation (supporting); Software (equal). **Zhe Jia**: Funding acquisition (supporting); Writing – review & editing (lead). **Baolong Shen**: Funding acquisition (lead); Supervision (lead); Writing – review & editing (equal).

DATA AVAILABILITY

The data that support the findings of this study are available from the corresponding authors upon reasonable request.

REFERENCES

[1] A. F. Ghoniem, "Needs, resources and climate change: Clean and efficient conversion technologies," Prog. Energy Combust. Sci. **37**(1), 15–51 (2011).

[2] X. Wang, W. Guo, and Y. Fu, "High-entropy alloys: Emerging materials for advanced functional applications," J. Mater. Chem. A **9**(2), 663–701 (2021).

[3] T. A. A. Batchelor, J. K. Pedersen, S. H. Winther, I. E. Castelli, K. W. Jacobsen, and J. Rossmeisl, "High-entropy alloys as a discovery platform for electrocatalysis," Joule **3**(3), 834–845 (2019).

[4] S. Anantharaj and S. Noda, "Amorphous catalysts and electrochemical water splitting: An untold story of harmony," Small **16**(2), e1905779 (2020).

[5] W. Dai, T. Lu, and Y. Pan, "Novel and promising electrocatalyst for oxygen evolution reaction based on MnFeCoNi high entropy alloy," J. Power Sources **430**, 104–111 (2019).

[6] Y. Jiao, Y. Zheng, M. Jaroniec, and S. Z. Qiao, "Design of electrocatalysts for oxygen- and hydrogen-involving energy conversion reactions," Chem. Soc. Rev. **44**(8), 2060–2086 (2015).

[7] K. Li and W. Chen, "Recent progress in high-entropy alloys for catalysts: Synthesis, applications, and prospects," Mater. Today Energy **20**, 100638 (2021).

[8] J. K. Pedersen, T. A. A. Batchelor, A. Bagger, and J. Rossmeisl, "High-entropy alloys as catalysts for the CO_2 and CO reduction reactions," ACS Catal. **10**(3), 2169–2176 (2020).

[9] Y. Xin, S. Li, Y. Qian, W. Zhu, H. Yuan, P. Jiang, R. Guo, and L. Wang, "High-entropy alloys as a platform for catalysis: Progress, challenges, and opportunities," ACS Catal. **10**(19), 11280–11306 (2020).

[10] Y. Ma, Y. Ma, Q. Wang, S. Schweidler, M. Botros, T. Fu, H. Hahn, T. Brezesinski, and B. Breitung, "High-entropy energy materials: Challenges and new opportunities," Energy Environ. Sci. **14**(5), 2883–2905 (2021).

[11] A. Amiri and R. Shahbazian-Yassar, "Recent progress of high-entropy materials for energy storage and conversion," J. Mater. Chem. A **9**(2), 782–823 (2021).

[12] Z. Jia, K. Nomoto, Q. Wang, C. Kong, L. Sun, L. C. Zhang, S. X. Liang, J. Lu, and J. J. Kruzic, "A self-supported high-entropy metallic glass with a nanosponge architecture for efficient hydrogen evolution under alkaline and acidic conditions," Adv. Funct. Mater. **31**(38), 2101586 (2021).

[13] J. Johny, Y. Li, M. Kamp, O. Prymak, S. X. Liang, T. Krekeler, M. Ritter, L. Kienle, C. Rehbock, S. Barcikowski, and S. Reichenberger, "Laser-generated high entropy metallic glass nanoparticles as bifunctional electrocatalysts," Nano Res. **15**, 4807–4819 (2021).

[14] G. Zhang, K. Ming, J. Kang, Q. Huang, Z. Zhang, X. Zheng, and X. Bi, "High entropy alloy as a highly active and stable electrocatalyst for hydrogen evolution reaction," Electrochim. Acta **279**, 19–23 (2018).

[15] Q. Wang, J. Li, Y. Li, and G. Shao, "Non-noble metal-based amorphous high-entropy oxides as efficient and reliable electrocatalysts for oxygen evolution reaction," Nano Res. **15**, 8751–8759 (2022).

[16] H. Li, Y. Han, H. Zhao, W. Qi, D. Zhang, Y. Yu, W. Cai, S. Li, J. Lai, B. Huang, and L. Wang, "Fast site-to-site electron transfer of high-entropy alloy nanocatalyst driving redox electrocatalysis," Nat. Commun. **11**(1), 5437 (2020).

[17] Z. Li, X. Wang, J. Ren, and H. Wang, "NiFe LDH/$Ti_3C_2T_x$/nickel foam as a binder-free electrode with enhanced oxygen evolution reaction performance," Int. J. Hydrogen Energy **47**(6), 3886–3892 (2022).

[18] Q. Qian, Y. Li, Y. Liu, L. Yu, and G. Zhang, "Ambient fast synthesis and active sites deciphering of hierarchical foam-like trimetal–organic framework nanostructures as a platform for highly efficient oxygen evolution electrocatalysis," Adv. Mater. **31**(23), 1901139 (2019).

[19] G. Shao, Q. Wang, F. Miao, J. Li, Y. Li, and B. Shen, "Improved catalytic efficiency and stability by surface activation in Fe-based amorphous alloys for hydrogen evolution reaction in acidic electrolyte," Electrochim. Acta **390**, 138815 (2021).

[20] S. Jiang, L. Zhu, Z. Yang, and Y. Wang, "Enhanced electrocatalytic performance of FeNiCoP amorphous alloys as oxygen-evolving catalysts for electrolytic water splitting application," Electrochim. Acta **368**, 137618 (2021).

[21] X. L. Liu, R. Wang, M. Y. Zhang, Y. P. Yuan, and C. Xue, "Dye-sensitized MIL-101 metal organic frameworks loaded with Ni/NiO_x nanoparticles for efficient visible-light-driven hydrogen generation," APL Mater. **3**(10), 104403 (2015).

[22] Q. Wang, M. Chen, P. Lin, Z. Cui, C. Chu, and B. Shen, "Investigation of FePC amorphous alloys with self-renewing behaviour for highly efficient decolorization of methylene blue," J. Mater. Chem. A **6**, 10686 (2018).

[23] Z. J. Chen, T. Zhang, X. Y. Gao, Y. J. Huang, X. H. Qin, Y. F. Wang, K. Zhao, X. Peng, C. Zhang, L. Liu, M. H. Zeng, and H. B. Yu, "Engineering microdomains of oxides in high-entropy alloy electrodes toward efficient oxygen evolution," Adv. Mater. **33**(33), 2101845 (2021).

[24] S. Ju, J. Feng, P. Zou, W. Xu, S. Wang, W. Gao, H.-J. Qiu, J. Huo, and J.-Q. Wang, "A robust self-stabilized electrode based on Al-based metallic glasses for a highly efficient hydrogen evolution reaction," J. Mater. Chem. A **8**(6), 3246–3251 (2020).

[25] R. Q. Yao, Y. T. Zhou, H. Shi, W. B. Wan, Q. H. Zhang, L. Gu, Y. F. Zhu, Z. Wen, X. Y. Lang, and Q. Jiang, "Nanoporous surface high-entropy alloys as highly efficient multisite electrocatalysts for nonacidic hydrogen evolution reaction," Adv. Funct. Mater. **31**(10), 2009613 (2020).

[26] P. Liu, Q. Chen, Y. Ito, J. Han, S. Chu, X. Wang, K. M. Reddy, S. Song, A. Hirata, and M. Chen, "Dealloying kinetics of AgAu nanoparticles by *in situ* liquid-cell scanning transmission electron microscopy," Nano Lett. **20**(3), 1944–1951 (2020).

[27] C. Pei, S. Chen, T. Zhao, M. Li, Z. Cui, B. Sun, S. Hu, S. Lan, H. Hahn, and T. Feng, "Nanostructured metallic glass in a highly upgraded energy state contributing to efficient catalytic performance," Adv. Mater. **34**(26), 2200850 (2022).

[28] Z. Jia, Y. Zhao, Q. Wang, F. Lyu, X. Tian, S.-X. Liang, L.-C. Zhang, J. Luan, Q. Wang, L. Sun, T. Yang, and B. Shen, "Nanoscale heterogeneities of non-noble iron-based metallic glasses toward efficient water oxidation at industrial-level current densities," ACS Appl. Mater. Interfaces **14**(8), 10288–10297 (2022).

[29] Y. Zhang, T. Lu, Y. Ye, W. Dai, Y. a. Zhu, and Y. Pan, "Stabilizing oxygen vacancy in entropy-engineered $CoFe_2O_4$-type catalysts for co-prosperity of efficiency and stability in an oxygen evolution reaction," ACS Appl. Mater. Interfaces **12**(29), 32548–32555 (2020).

[30] Z. Ding, J. Bian, S. Shuang, X. Liu, Y. Hu, C. Sun, and Y. Yang, "High entropy intermetallic–oxide core–shell nanostructure as superb oxygen evolution reaction catalyst," Adv. Sustainable Syst. **4**(5), 1900105 (2020).

[31] G. Fang, J. Gao, J. Lv, H. Jia, H. Li, W. Liu, G. Xie, Z. Chen, Y. Huang, Q. Yuan, X. Liu, X. Lin, S. Sun, and H.-J. Qiu, "Multi-component nanoporous alloy/(oxy)hydroxide for bifunctional oxygen electrocatalysis and rechargeable Zn-air batteries," Appl. Catal. B **268**, 118431 (2020).

[32] Z. Jin, J. Lyu, Y.-L. Zhao, H. Li, X. Lin, G. Xie, X. Liu, J.-J. Kai, and H.-J. Qiu, "Rugged high-entropy alloy nanowires with in situ formed surface spinel oxide as highly stable electrocatalyst in Zn–air batteries," ACS Mater. Lett. **2**(12), 1698–1706 (2020).

[33]H. Liu, H. Qin, J. Kang, L. Ma, G. Chen, Q. Huang, Z. Zhang, E. Liu, H. Lu, J. Li, and N. Zhao, "A freestanding nanoporous NiCoFeMoMn high-entropy alloy as an efficient electrocatalyst for rapid water splitting," Chem. Eng. J. **435**, 134898 (2022).
[34]Z. Jia, T. Yang, L. Sun, Y. Zhao, W. Li, J. Luan, F. Lyu, L. C. Zhang, J. J. Kruzic, J. J. Kai, J. C. Huang, J. Lu, and C. T. Liu, "A novel multinary intermetallic as an active electrocatalyst for hydrogen evolution," Adv. Mater. **32**(21), 2000385 (2020).
[35]J. Lin, Y. Yan, C. Li, X. Si, H. Wang, J. Qi, J. Cao, Z. Zhong, W. Fei, J. Feng, "Bifunctional electrocatalysts based on Mo-doped NiCoP nanosheet arrays for overall water splitting," Nano-Micro Lett. **11**(1), 55 (2019).
[36]H. Mao, X. Guo, Y. Fu, H. Yang, Y. Zhang, R. Zhang, and X.-M. Song, "Enhanced electrolytic oxygen evolution by the synergistic effects of trimetallic FeCoNi boride oxides immobilized on polypyrrole/reduced graphene oxide," J. Mater. Chem. A **8**(4), 1821–1828 (2020).
[37]J. M. V. Nsanzimana, R. Dangol, V. Reddu, S. Duo, Y. Peng, K. N. Dinh, Z. Huang, Q. Yan, and X. Wang, "Facile synthesis of amorphous ternary metal borides-reduced graphene oxide hybrid with superior oxygen evolution activity," ACS Appl. Mater. Interfaces **11**(1), 846–855 (2019).
[38]J. Kibsgaard and I. Chorkendorff, "Considerations for the scaling-up of water splitting catalysts," Nat. Energy **4**(6), 430–433 (2019).